Rare Metal Materials and Engineering
Volume 55, Issue 10, October 2026
Available online at www.rmme.ac.cn

Science Press

Cite this article as: Ding Shaoling, Wu Ming, Shi Shuangxi, et al. A Strain-Compensated Arrhenius Model for TC18 Alloy Optimized via Genetic Algorithm and Response Surface Methodology[J]. Rare Metal Materials and Engineering, 2026, 55(10): 2429-2441. DOI: https://doi.org/10.12442/j.issn.1002-185X.20250547.

ARTICLE

A Strain-Compensated Arrhenius Model for TC18 Alloy Optimized via Genetic Algorithm and Response Surface Methodology

Ding Shaoling[1], Wu Ming[1], Shi Shuangxi[2,3], An Hui[1], Zhang Yong[2,3]

[1] School of Mathematics and Statistics, Guilin University of Technology, Guilin 541006, China; [2] Guangxi Key Laboratory of Special Engineering Equipment and Control, Guilin University of Aerospace Technology, Guilin 541004, China; [3] Guangxi Region Precious Metal Materials Advanced Process Research Center, Guilin University of Aerospace Technology, Guilin 541004, China

Abstract: Accurate prediction of hot deformation behavior is critical for numerical simulation and intelligent manufacturing of titanium alloy forgings. The high-temperature deformation characteristics of TC18 titanium alloy were investigated using isothermal compression tests on a Gleeble-3800 thermal simulator over the temperature range of 720–840 °C and strain rate range of 0.001–1 s^{-1}. To precisely describe the flow behavior, three strain-compensated Arrhenius (SCA) constitutive models were developed and evaluated: a linear regression-fitted SCA (LR-SCA) model, a genetic algorithm-optimized SCA (GA-SCA) model, and a response surface-modified SCA (RS-SCA) model. The results demonstrate that genetic algorithm optimization effectively identifies global optimal parameters, while the response surface modification successfully accounts for the coupling effects of temperature and strain rate. Statistical evaluation reveals that the RS-SCA model achieves superior predictive capability, with a correlation coefficient (R) of 0.9980 and a mean absolute relative error of 2.16%, a significant improvement over the LR-SCA model's 7.01%. The reliability of the established RS-SCA model is further validated through its secondary development in DEFORM-3D, where finite-element simulations under stable processing conditions show excellent agreement with experimental load-displacement curves. This robust constitutive model provides a solid foundation for finite element simulation and process optimization of TC18 alloy components in thermomechanical processing applications.

Key words: TC18 alloy; flow stress; hot deformation behavior; Arrhenius constitutive model; finite element simulation

1 Introduction

Ti alloys are widely used in aerospace, marine, biomedicine, and other fields due to their high specific strength, good impact and fracture toughness, and excellent corrosion resistance[1–3]. TC18 is a typical near-β series high-strength and high-toughness Ti alloy, with excellent weldability and hardenability, making it ideal for the manufacture of large bearing components such as landing gears, fuselages, and rotor systems for airplanes, thereby ensuring safety in service and reducing mass[4–5]. Due to its low room-temperature plasticity, TC18 alloy is primarily processed by thermomechanical processing (TMP) to produce Ti alloy billets/forgings[6].

The hot deformation behavior of the alloys during processing is very complex. It depends not only on the initial microstructure but also on the competing hardening and softening behavior during deformation, which are significantly affected by thermodynamic parameters such as deformation temperature, strain, and strain rate[7–9]. The flow stress constitutive model and hot-working maps are the primary means of investigating the hot deformation behavior of alloys and provide an important basis for guiding the iterative optimization of forging processes. For example, the flow stress of the alloy determines the processing equipment tonnage, and the kinetic parameters such as deformation

Received date: October 25, 2025
Foundation item: National Natural Science Foundation of China (52461004); Guangxi Natural Science Foundation (2025GXNSFAA069352)
Corresponding author: Shi Shuangxi, Ph. D., Professor, Guangxi Key Laboratory of Special Engineering Equipment and Control, Guilin University of Aerospace Technology, Guilin 541004, P. R. China, E-mail: shishxi2023@guat.edu.cn

activation energy, strain-hardening index, temperature sensitivity index, and strain-rate sensitivity index in the constitutive equations reflect the difficulty and influence law of TMP. The hot working diagram identifies the workable and unstable intervals of the alloy and provides a theoretical basis for practical forging production[10–11]. Furthermore, finite element (FE) simulations based on constitutive models can predict thermoplastic flow patterns and defects during the TMP process. They can further iteratively optimize the TMP process for the alloy, thereby enabling intelligent manufacturing of Ti-alloy aerospace forgings[12]. Therefore, it is imperative to thoroughly study the hot deformation behavior of near-β Ti alloys and develop constitutive models that accurately describe their flow behavior.

In recent years, many researchers have attempted to develop deformation constitutive models based on experimental data to describe the hot deformation behavior of Ti alloys accurately. These models can be roughly categorized into physical, phenomenological, and machine-learning models[13–15]. Physical models coupled with complex microstructural evolution laws and deformation mechanisms make the establishment process cumbersome. In addition, the modeling process often simplifies the underlying physical metallurgical processes, making it difficult to ensure the model's predictive accuracy and thereby limiting its applications[16–17]. Wu[18] and Bobbili[19] et al established physical models to describe the hot deformation behavior of Ti2AlNb and Ti-5Al-4Sn-2Zr-5Mo alloys, respectively, based on dislocation motion and diffusion mechanisms; the relative differences between the predicted and experimental flow stresses are 7.6% – 11.4% and 8.65%, respectively. The phenomenological models are widely used in TMP due to their applicability, simplicity of solution, and ease of secondary development. Representative models are Arrhenius[20], Johnson-Cook[21], Zerilli-Armstrong[22], and Field-Backofen[23], which partially or fully couple the effects of temperature, strain rate, and strain hardening or softening. Among them, the Arrhenius phenomenological model proposed by Sellars and McTegart is the most widely used and maps flow stresses as a hyperbolic sine function of thermodynamic parameters[24]. Machine-learning methods such as artificial neural networks (ANNs) and support vector regression (SVR) have demonstrated strong performance and high accuracy in solving complex nonlinear problems[25–26]. Qi[27] et al developed sparrow search algorithm-optimized SVR constitutive models to describe the flow behavior of TC4 alloys, achieving an average absolute relative error (AARE) of 5.12%. Deng et al[28] optimized Arrhenius constants for a β Ti alloy via genetic algorithm (GA), achieving high accuracy, and both machine-learning and optimized phenomenological models effectively capture hot deformation. However, to the best of our knowledge, most machine-learning models in previous studies treat the TMP process parameters as inputs and the flow stresses as outputs, and do not describe specific physical mechanisms or implications[29]. In addition, machine-learning models are difficult to develop further. The complex topological network structure will prolong computational time and consume resources during simulation, and the models may converge to local optima[30]. Machine-learning models are not suitable for practical application in the TMP simulation process. Therefore, it is necessary to develop an Arrhenius model that accurately predicts flow stress, is convenient for secondary FE simulations, and has a clear physical interpretation.

However, the original Arrhenius model did not account for the effect of strain on the flow stress. In fact, the flow stress usually varies with strain hardening or softening, especially when microstructural evolution, such as lamellar α-spheroidization, dynamic recovery (DRV), and dynamic recrystallization (DRX), occurs. Low model prediction accuracy leads to deviations in FE simulation results. To improve the accuracy of the Arrhenius model and its application, many scholars have used multiple linear regression (LR) methods to develop a strain-compensated improved model. Chai[31] and Wang[32] et al developed polynomial strain-compensated Arrhenius (SCA) models using multiple linear LR to predict flow stresses in TC11 and as-cast Ti-5Al-5Mo-5V-1Cr-1Fe alloys. Although the overall accuracy of the Arrhenius model has improved, the deviation between predicted and experimental values remains greater than 10% for many thermodynamic parameters[33]. Therefore, this work aims to further refine the SCA model and improve its predictive accuracy, particularly in parameter estimation and the coupling among thermodynamic parameters. Existing studies have not combined GA and response surface (RS) methodology for modifying the SCA model of Ti alloys to simultaneously address local optimization and the neglect of coupling effects; based on this, this work applies GA and RS in combination to modify the SCA model, which provides three distinct novel contributions beyond current research. First, GA is used for global parameter identification of the SCA model to overcome the local optimization defect of multiple LR, and to achieve this, GA identifies the optimal model parameters according to each strain without any gradient information or continuity assumptions, an advantage that has been widely validated in material parameter optimization for Ti alloys such as Ti-6554[34], Ti64[35], and TC6[36]. Second, RS is subsequently applied to the GA-optimized model to construct a temperature-strain rate correction function, which enables a quantitative description of the effect of the temperature-strain rate interaction on flow stress (a factor overlooked in conventional SCA models that focus only on the individual effect of strain). Third, the combined use of GA and RS reduces the model's AARE to less than 5%, thereby enhancing its reliability in FE simulation of Ti alloy thermal deformation behavior.

In this work, three modified SCA models were developed and compared through a series of statistical analyses. Specifically, first, the stress-strain data of TC18 alloy over the temperature range of 720 – 840 °C, with an interval of 40 °C, and the strain rate range of 0.001 – 1 s^{-1} were obtained from isothermal compression tests conducted on a Gleeble-

3800 thermal simulator. Second, the thermoplastic flow characteristics of the alloy were analyzed from stress-strain curves. Third, three SCA models were developed using multiple LR, GA, and RS modification methods, namely LR-SCA, GA-SCA, and RS-SCA models. Four statistical indicators, such as the correlation coefficient (R), AARE, the logarithm of mean squared error (ln(MSE)), and relative error (η), were used to compare and to evaluate the prediction performance of the three models. Finally, the established SCA model was further developed in DEFORM 3D software to verify its validity and reliability. Our findings might further help understand the deformation behavior of TC18 alloy and provide data support for the numerical simulation of TMP.

2 Experiment

2.1 Materials

The nominal chemical composition of TC18 alloy used in this investigation is detailed in Table 1, and its β-transus temperature (T_β) is approximately 875±5 °C, as reported in Ref.[12,29]. The initial microstructure consisted of lamellar α phase and a matrix, as shown in Fig.1a. The thickness of the α phase is 0.2−0.5 μm, which accounts for roughly 50% of the volume. Besides, the lamellar α phase is approximately triangular and uniformly distributed in the β matrix.

2.2 Hot compression test and observation

The hot compression tests of TC18 alloy were performed on a Gleeble-3800 thermomechanical simulator with resistance heating. The specimens were cylindrical, with dimensions of Φ10 mm×15 mm. The experimental process consisted of three stages: heating and holding, thermal deformation, and cooling. The specimen was heated at 10 °C/s and held for 180 s to ensure uniform temperature distribution. The testing temperatures were 720, 760, 800, and 840 °C, and the strain rates were 0.001, 0.01, 0.1, and 1 s^{-1}. The total strain was 0.9. Before testing, argon gas was passed through to protect the specimens from oxidation, and thin graphite and tantalum sheets were placed between the specimens and the anvil to reduce friction. The specimen was water-cooled immediately after compression to retain the deformed microstructure. The true stress-true strain curve was recorded automatically. The specific procedure is shown in Fig.1b.

Table 1 Chemical composition of TC18 alloy (wt%)

Al	Mo	V	Cr	Fe	Ti
5.16	4.92	4.96	1.10	0.98	Bal.

The compressed specimens were sliced along the compression direction, and their surfaces were polished to a mirror finish. Samples were prepared by etching and electropolishing for microstructural characterization, as detailed in Ref. [37]. The central region of the samples was observed using a scanning electron microscope (SEM, Helios NanoLab G3 UC) equipped with an electron backscatter diffraction (EBSD) detector. EBSD data were post-processed using TSL-OIM 6.0.

3 Results

3.1 Hot deformation behavior

The flow stress profiles of TC18 alloy at different deformation temperatures (720, 760, 800, and 840 °C) and strain rates (0.001, 0.01, 0.1 and 1 s^{-1}) are shown in Fig.2. It is found that there is a significant correlation between the flow stress of the alloy and thermodynamic parameters: the flow stress decreases with increasing deformation temperature and increases with increasing strain rate. Such characteristics of flow stress curves can also be observed in other Ti alloys[38–40]. In high-temperature deformation, the higher the atoms' kinetic energy, the lower the critical shear stress for interatomic interactions. The sliding resistance of the dislocations decreases, and the alloy's deformation resistance thus decreases. In addition, the alloy is more susceptible to dynamic softening at high temperatures due to microstructural evolution, such as DRV and DRX, and its thermoplasticity is enhanced. At the same time, its deformation resistance is reduced[12]. The effect of strain rate on flow stress can be explained by the dislocation dynamics equation[41]. The higher the strain rate, the faster the dislocation migration and the stronger the required driving force. The trend of flow stress versus strain under different deformation conditions shows that the stress rapidly reaches a peak in the initial stage, then gradually decreases, and eventually converges to a steady-state value. In other words, the dynamic softening effect of DRV is weak in the early stage of deformation, and the flow stress increases rapidly due to work hardening caused by

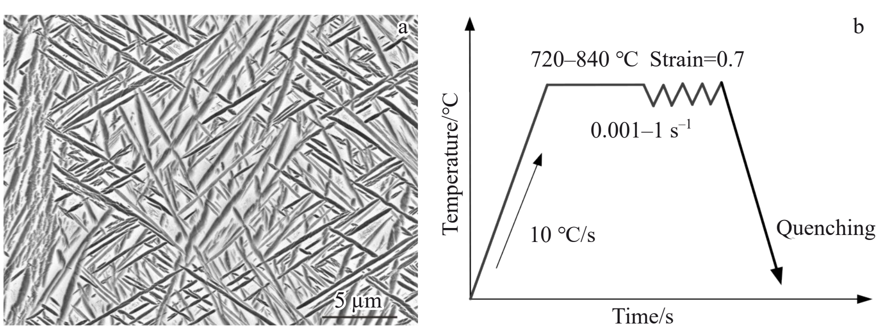

Fig.1 Initial microstructure (a) and experimental route (b) of TC18 alloy

dislocation proliferation and entanglement. As the strain increases to the critical strain, the DRX-induced dynamic softening effect is enhanced, and the flow stress increases slowly. The flow stress peaks when work hardening and dynamic softening reach equilibrium. With the further increase in strain, the degree of DRX increases; the dynamic softening effect, including DRV and DRX, exceeds the work-hardening effect, and the flow stress decreases[42]. Finally, a steady-state flow phase occurs at large strains, driven by a dynamic balance between strain hardening and dynamic softening.

Fig. 3a shows the peak flow stress as a function of various thermodynamic parameters. Its maximum value is 438.36 MPa at 720 °C/1 s^{-1} and decreases to 38.28 MPa at 840 °C/ 0.001 s^{-1}. At low temperatures and high strain rates, atomic kinetic energy is low, and dislocation motion is relatively difficult. The time required to reach critical strain is reduced, and the rate of dislocation proliferation increases. Therefore, the alloy's resistance to deformation increases. On the contrary, at high temperatures and low strain rates, the kinetic energy of atoms increases, and dislocation motion becomes easier. In addition, as the content of the β phase with more slip systems increases, and the content of the hard α phase decreases, the ductility of the alloy increases, and the deformation resistance decreases. The flow softening extent ($\Delta\sigma$), defined as the difference between the peak flow stress (σ_{peak}) and the steady-state flow stress (σ_{ss}) in the stress-strain curve, is presented in Fig. 3b under different thermodynamic parameters. $\Delta\sigma$ follows a trend similar to peak stress, decreasing with increasing deformation temperature and decreasing strain rate. Previous studies have shown that the flow softening of Ti alloys with a lamellar structure may be caused by microstructural evolution and the heat of deformation, either alone or in combination[43]. Microstructural evolution, including DRX, DRV, bending, and spheroidization of lamellar α, as well as texture changes, is a key factor in the dynamic softening of the alloy[44–45].

3.2 LR-SCA

The Arrhenius constitutive model proposed by Sellars and McTegart is commonly used to describe the deformation

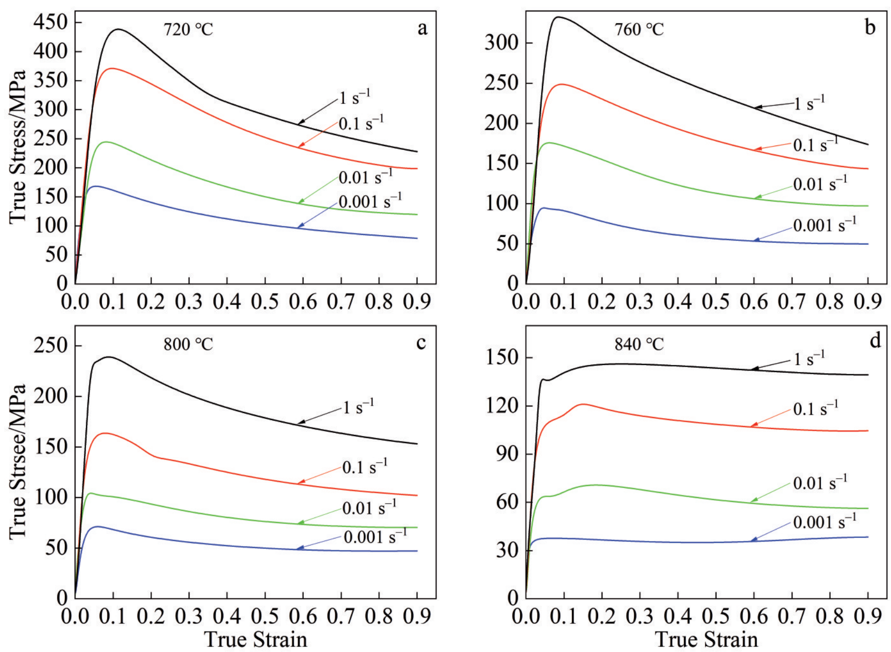

Fig.2 Flow curves of TC18 alloy under different thermodynamic parameters: (a) 720 °C; (b) 760 °C; (c) 800 °C; (d) 840 °C

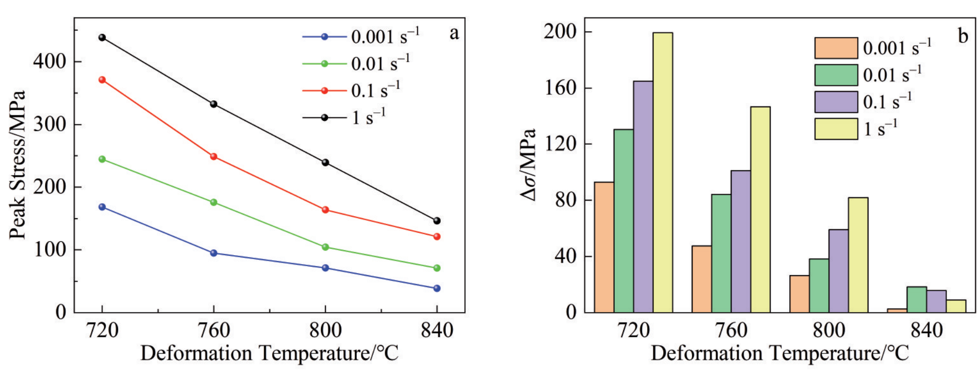

Fig.3 Peak stress (a) and flow softening extent $\Delta\sigma$ (b) of TC18 alloy under different thermodynamic parameters

behavior of materials at elevated temperatures, particularly the processes related to temperature, stress, or strain rate[20]. The model is widely used in materials science, metallurgy, and mechanical engineering to study the hot deformation behavior of materials under mechanical loading. The mathematical framework is generally described by a hyperbolic sine function of the deformation temperature and the deformation activation energy, as shown in Eq.(1)[46].

$$\dot{\varepsilon} = \begin{cases} A[\sinh(\alpha\sigma)]^n \exp[-Q/(RT)] & \text{for all } \sigma \\ A_1\sigma^{n_1}\exp[-Q/(RT)] & \alpha\sigma \leqslant 0.8 \\ A_2\exp(\beta\sigma)\exp[-Q/(RT)] & \alpha\sigma > 0.8 \end{cases} \quad (1)$$

where A, A_1, A_2, n, α, n_1, and β are the material constants and $\alpha=\beta/n_1$; $\dot{\varepsilon}$ is the strain rate (s^{-1}); σ is the flow stress (MPa); T is the deformation temperature (K); R is the gas constant (8.314 $J\cdot mol^{-1}\cdot K^{-1}$); Q is the deformation activation energy ($kJ\cdot mol^{-1}$).

Taking natural logarithms on both sides of Eq.(1), Eq.(2) can be obtained by rearranging:

$$\ln\dot{\varepsilon} = \begin{cases} \ln A + n\ln[\sinh(\alpha\sigma)] - Q/(RT) \\ \ln A_1 + n_1\ln\sigma - Q/(RT) \\ \ln A_2 + \beta\sigma - Q/(RT) \end{cases} \quad (2)$$

According to Eq. (2), the constants β and n_1 can be determined from the slopes of the $\ln\dot{\varepsilon}$-σ curve and the $\ln\dot{\varepsilon}$-$\ln\sigma$ curve, respectively. Therefore, the value of α can be calculated. The constant n can be determined from the slope of the $\ln\dot{\varepsilon}$-$\ln[\sinh(\alpha\sigma)]$ curve. By taking the second-order partial derivative of the first expression in Eq.(2), the Q/nR value can be derived from the slope of the $\ln[\sinh(\alpha\sigma)]$-$(1000/T)$ curve. The value of $\ln A$ can be calculated from the intercept of the $\ln\dot{\varepsilon}+Q/nR$-$\ln[\sinh(\alpha\sigma)]$ curve. The peak stresses (σ_p) at different thermodynamic parameters were selected and plotted as linear fits to $\ln\dot{\varepsilon}$-σ_p, $\ln\dot{\varepsilon}$-$\ln\sigma_p$, $\ln\dot{\varepsilon}$-$\ln[\sinh(\alpha\sigma_p)]$, $\ln[\sinh(\alpha\sigma_p)]$-$(1000/T)$, and $\ln\dot{\varepsilon}+Q/nR$-$\ln[\sinh(\alpha\sigma_p)]$, as shown in Fig.4. The values of β=0.0385 and n_1=5.6717 MPa^{-1} are determined by averaging the slopes of the fitting lines in Fig.4a and 4b, resulting in α=0.0068 MPa^{-1}. By averaging the slopes of the fitting lines in Fig.4c and 4d, the values of n=3.9284 and Q/nR=16.8098 are determined, resulting in Q=549.0186 $kJ\cdot mol^{-1}$. The Q value can be used as an index to characterize the ease of hot deformation. The $\ln A$ value of 57.8629 is determined based on the intercept of the fitted line in Fig.4e. At this point, all parameters in the constitutive model have been solved.

According to the definition of the hyperbolic sine function, the relationship between σ and T is obtained as:

$$\sigma = \frac{1}{\alpha}\ln\left(\left[\frac{\dot{\varepsilon}\exp(Q/RT)}{A}\right]^{1/n} + \left\{\left[\frac{\dot{\varepsilon}\exp(Q/RT)}{A}\right]^{2/n} + 1\right\}^{1/2}\right) \quad (3)$$

$$\sigma_p = \frac{1}{0.0068}\ln\left(\left[\frac{\dot{\varepsilon}\exp(549.0186/RT)}{1.3475\times10^{25}}\right]^{\frac{1}{3.9284}} + \left\{\left[\frac{\dot{\varepsilon}\exp(549.0186/RT)}{1.3475\times10^{25}}\right]^{\frac{2}{3.9284}} + 1\right\}^{\frac{1}{2}}\right) \quad (4)$$

Eventually, the peak-stress Arrhenius-type constitutive model for the TC18 alloy is derived by substituting the material parameters into Eq.(3), as shown in Eq.(4).

The above model can only capture the constitutive

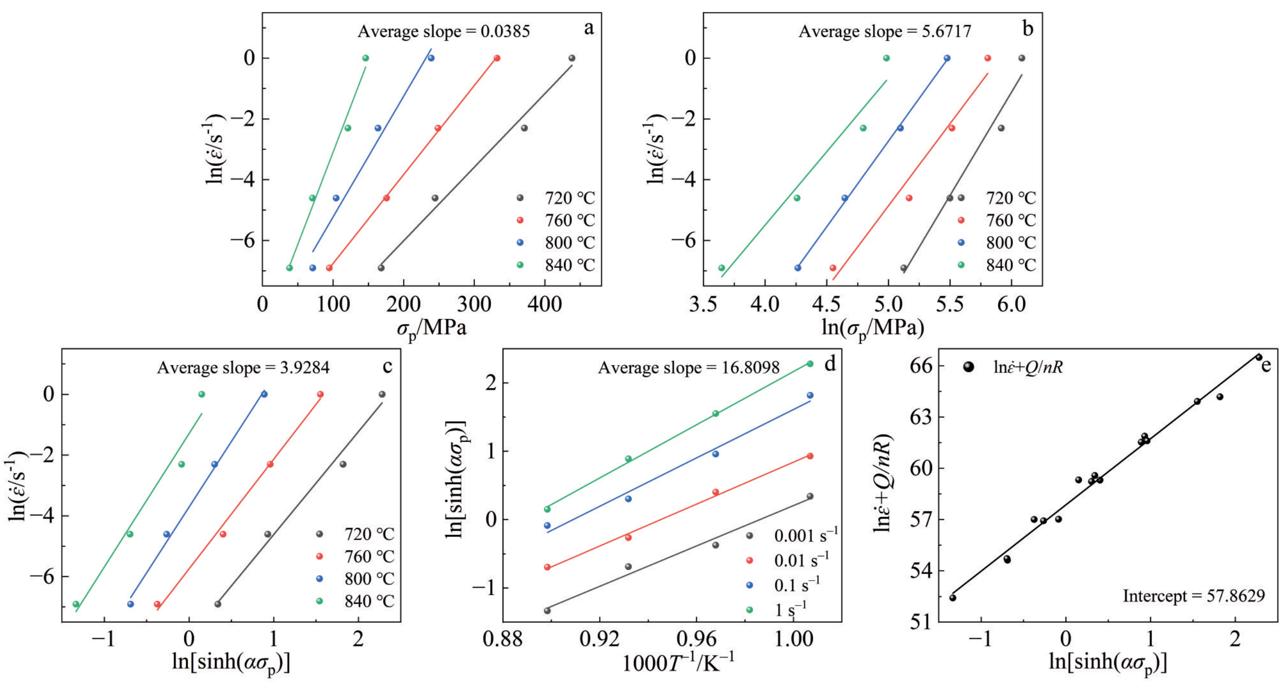

Fig.4 Linear fit between peak stress (σ_p) and thermodynamic parameters: (a) $\ln\dot{\varepsilon}$-σ_p, (b) $\ln\dot{\varepsilon}$-$\ln\sigma_p$, (c) $\ln\dot{\varepsilon}$–$\ln[\sinh(\alpha\sigma_p)]$, (d) $\ln[\sinh(\alpha\sigma_p)]$-$(1000/T)$, and (e) $\ln\dot{\varepsilon}+Q/nR$-$\ln[\sinh(\alpha\sigma_p)]$

relationship under peak-stress conditions. The Arrhenius model does not account for the influence of strain on flow stress. However, previous studies have shown that microstructural evolution and thermal deformation during hot deformation of lamellar TC18 alloy can lead to flow softening, with flow stress typically varying with strain[12,29,37]. In the early stages of deformation, when the strain is small, work hardening dominates. As the strain increases, microstructural softening behavior such as DRV, DRX, and lamellar spheroidization occurs, thereby making subsequent deformation easier[42]. Therefore, the influence of strain on flow stress must be considered in the constitutive model for the thermoplastic deformation of TC18 alloy. To improve the applicability of the Arrhenius model over a wide range of strains, these model parameters are evaluated at more strain levels, and an SCA model is established. The material parameters corresponding to strain intervals of 0.05 in the strain range of 0.1–0.9 were determined. The results show that strain has a significant, nonlinear effect on the model parameters. Therefore, an nth-order polynomial is used to describe the functional relationship between the model parameters and strain.

To determine the order of the polynomial, adjustment coefficients are used to evaluate the fitting performance of 1st-to 9th-order polynomials. Fig. 5 illustrates the effect of polynomial order on the parameter fitting performance of the SCA model. As the order of the polynomial increases, the value of adjusted R-squared (Adj. R^2) also increases. However, when the order exceeds 8, the increase in Adj. R^2 decreases sharply. Therefore, a 9th-order polynomial is chosen to fit the model parameters. The Adj. R^2 of the polynomial fit for material parameters α, n, Q, and ln$A$ to strains is 1, 0.990 80, 0.999 67, and 0.999 67, respectively, indicating a better fit.

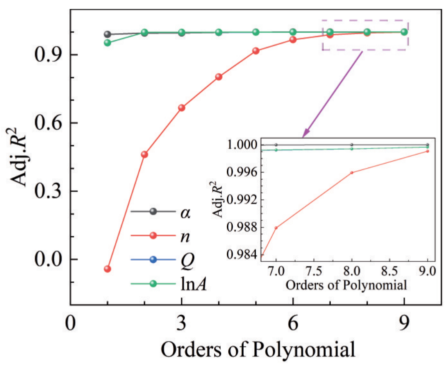

Fig.5 Analysis of the number of fitting orders

As shown in Fig. 6, the relationships between model parameters (α, n, Q, ln$A$) and strain are fitted by 9th-order polynomials, and the detailed expression is described by Eq. (5). Table 2 lists the fitting coefficients of the 9th-order polynomial. Substituting Eq. (5) into Eq. (3), the expression of the SCA model for the TC18 alloy can be expressed as Eq. (6).

$$\begin{cases} \alpha(\varepsilon) = B_0 + B_1\varepsilon + B_2\varepsilon^2 + B_3\varepsilon^3 + B_4\varepsilon^4 + B_5\varepsilon^5 + B_6\varepsilon^6 + B_7\varepsilon^7 + B_8\varepsilon^8 + B_9\varepsilon^9 \\ n(\varepsilon) = C_0 + C_1\varepsilon + C_2\varepsilon^2 + C_3\varepsilon^3 + C_4\varepsilon^4 + C_5\varepsilon^5 + C_6\varepsilon^6 + C_7\varepsilon^7 + C_8\varepsilon^8 + C_9\varepsilon^9 \\ Q(\varepsilon) = D_0 + D_1\varepsilon + D_2\varepsilon^2 + D_3\varepsilon^3 + D_4\varepsilon^4 + D_5\varepsilon^5 + D_6\varepsilon^6 + D_7\varepsilon^7 + D_8\varepsilon^8 + D_9\varepsilon^9 \\ \ln A(\varepsilon) = E_0 + E_1\varepsilon + E_2\varepsilon^2 + E_3\varepsilon^3 + E_4\varepsilon^4 + E_5\varepsilon^5 + E_6\varepsilon^6 + E_7\varepsilon^7 + E_8\varepsilon^8 + E_9\varepsilon^9 \end{cases} \tag{5}$$

$$\sigma = \frac{1}{\alpha(\varepsilon)} \ln\left[\left\{\frac{\dot{\varepsilon}\exp\left[Q(\varepsilon)/RT\right]}{A(\varepsilon)}\right\}^{1/n(\varepsilon)} + \left(\left\{\frac{\dot{\varepsilon}\exp\left[Q(\varepsilon)/RT\right]}{A(\varepsilon)}\right\}^{2/n(\varepsilon)} + 1\right)^{1/2}\right] \tag{6}$$

3.3 GA-SCA

Although the LR-SCA model can predict the hot deformation behavior of TC18 alloy well, its predictive accuracy is relatively low under high-temperature and high-strain-rate conditions (e.g., 800 °C/0.1 s^{-1} and 840 °C/1 s^{-1}). GA is a computational model that simulates biological evolution by replicating natural selection and genetic mechanisms of Darwinian evolution, and it can solve complex optimization problems[47–48]. GA encodes individuals onto chromosomes, randomly generates an initial population of a certain size, selects individuals based on fitness, and gradually evolves the optimal individual as the optimal solution using crossover and mutation of genetic factors.

To optimize the parameter set in the SCA model, which predicts the hot deformation behavior of TC18 alloy with high accuracy, a residual fitness function was introduced and denoted as[16]:

$$f_\sigma(x) = \frac{1}{L_\sigma}\sum_{k=1}^{L_\sigma}\left\{\frac{1}{M_k}\sum_{j=1}^{M_k}\left[\frac{1}{N_i}\sum_{i=1}^{N_i}\left(\ln\frac{\sigma_{ij}^{\mathrm{p}}}{\sigma_{ij}^{\mathrm{e}}}\right)^2\right]\right\} \tag{7}$$

where $f_\sigma(x)$ is the residual of the predicted value of flow stress relative to the experimental value; L is the number of predicted curves; M is the number of predicted curves at different strain rates at the same temperature; N is the number of points of curves at the same temperature and the same strain rate; x is the material parameter to be solved; σ_{ij}^{p} and σ_{ij}^{e} are the predicted and experimental values of flow stress at the same temperature at strain i and strain rate j, respectively. Furthermore, the upper and lower limits of the preset parameters α, n, Q, and ln$A$ are given according to the results of Section 3.2, and their values are 0.007 065 – 0.010 156 MPa^{-1}, 3.70 – 4.59, 294.13 – 564.39 kJ·mol^{-1}, and 29.18 – 59.76 s^{-1}, respectively. The mutation function is mutation-adapt feasible, the GA simulation parameters are set, as shown in Table 3, and the remaining settings use the default settings of the MATLAB toolbox.

Fig. 7 illustrates the flowchart for identifying the model parameters (α, n, Q, and ln$A$) in Eq. (3) using GA. In this process, the experimental data and model parameter ranges were first loaded, and four parameters within the preset ranges were

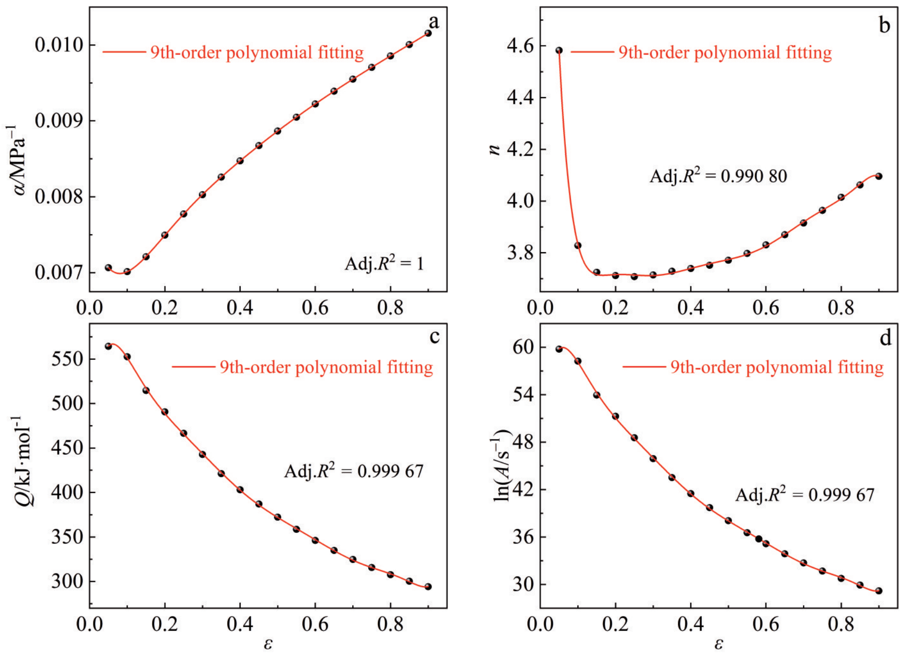

Fig.6 Fitted curves of the α (a), n (b), Q (c), and ln$A$ (d)

Table 2 Fitting coefficients of the 9th-order polynomials

B	α/MPa^{-1}	C	n	D	Q/kJ·mol^{-1}	E	ln(A/s^{-1})
B_0	0.007 7	C_0	7.432	D_0	453.605 2	E_0	48.096 8
B_1	–0.021 9	C_1	–96.197 7	D_1	4 887.083 2	E_1	522.362 4
B_2	0.225 1	C_2	1 046.664 0	D_2	74 996.400 7	E_2	–8 130.934 5
B_3	–0.949 6	C_3	6 279.243 6	D_3	528 667.818 0	E_3	57 603.119 6
B_4	2.266 1	C_4	22 914.136 0	D_4	2 163 794.650 0	E_4	236 482.698 0
B_5	–3.146 0	C_5	52 900.594 9	D_5	5 450 325.390 0	E_5	596 972.952 0
B_6	2.346 1	C_6	77 592.445 4	D_6	8 553 658.980 0	E_6	938 465.285 0
B_7	–0.598 1	C_7	70 028.533 6	D_7	8 143 310.900 0	E_7	894 653.272 0
B_8	–0.272 1	C_8	35 437.872 6	D_8	4 301 222.590 0	E_8	473 069.020 0
B_9	0.153 4	C_9	7 691.640 4	D_9	966 581.707 0	E_9	106 405.940 0

Table 3 Parameters of GA setting in the algorithm toolbox

Population size	Stopping generation	Allowable error	Crossover rate
200	4000	1×10^{-8}	0.9

randomly selected as the initial population and encoded on individual chromosomes. The corresponding flow stresses predicted by the SCA model were then calculated. Individual fitness values were calculated from the residuals of Eq.(7) and ranked by size. The chromosomes of individuals with lower fitness values were selected, crossed, and mutated to obtain the new population. Meanwhile, the new model parameters were obtained, and the corresponding stress values were calculated. If the iteration stopping condition is not satisfied, the process is repeated. Otherwise, the iteration is stopped, and the optimized model parameters with the lowest fitness values are obtained.

Table 4 shows the results of GA optimization at each strain level, and the residuals of the experimental values are all less than 0.0075, indicating that the optimized model parameters provide a better predictive accuracy. Finally, according to the strain compensation method in Section 3.2, the model parameters are also polynomially fitted, and the stress values of the alloy under each thermodynamic parameter can be predicted by substituting into Eq.(6).

3.4 RS-SCA

The model parameters were obtained by partial differentiation of the Arrhenius equation with respect to temperature and strain rate at a fixed strain, or by GA identification. The effects of temperature, strain rate, and their coupling effects were not considered. To minimize the deviation between the SCA model's calculated results and the experimental results, an RS-fitting function, $K_{ij}(\dot{\varepsilon}, T)$, is introduced to modify the SCA model. The modification factor for a given temperature and strain rate is determined by averaging the ratio of experimental stress to predicted stress across all strain levels at the specified thermodynamic

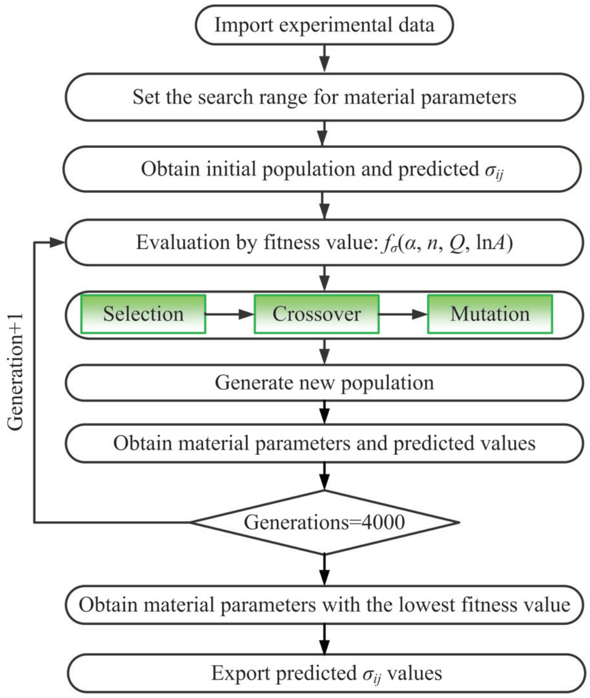

Fig.7 Flowchart of GA for solving model parameters

parameters, as shown in Eq.(8).

$$K_{ij}(\dot{\varepsilon}, T) = \frac{1}{n}\sum_{k=1}^{n}\frac{\sigma_{ijk}^{\mathrm{e}}}{\sigma_{ijk}^{\mathrm{p}}} \tag{8}$$

where i is the corresponding temperature condition; j is the corresponding strain rate condition; k is the number of strain levels under the corresponding thermodynamic parameters; $\sigma_{ijk}^{\mathrm{e}}$ and $\sigma_{ijk}^{\mathrm{p}}$ are the experimental and predicted stresses, respectively. The larger the value of K, the more significant the coupled effect of temperature and strain rate on the flow stress.

In this work, the model is developed by selecting data at 0.05-interval strain values in the range 0.05 – 0.90 at each deformation temperature and strain rate, and the K value is determined by averaging the ratios of the 18 predicted stresses to the experimental stresses. A total of 16 groups of K values are obtained at four deformation temperatures and four strain rates, as listed in Table 5.

The experimental stress, the predicted stress from the SCA model, and the modification function are all functions of thermodynamic parameters, and their relationship can be described by Eq.(9).

$$\sigma_{\mathrm{e}} = K_{ij}(\dot{\varepsilon}, T)\sigma_{\mathrm{p}} \tag{9}$$

The K values are subjected to nonlinear RS fitting, as shown in Fig. 8. The correction operator is a polynomial function of strain rate and deformation temperature. The fitted equation for the RS is Eq.(10).

Table 4 Optimal model parameters at each strain level with the lowest fitness values

ε	α/×10^{-2} MPa^{-1}	n	Q/k·mol^{-1}	ln(A/s^{-1})	f_σ
0.05	0.9139	4.0096	564.3900	58.2496	0.0048
0.10	0.7079	3.9054	525.2372	55.0805	0.0065
0.15	0.7065	3.8602	484.8639	50.6626	0.0073
0.20	0.7291	3.8691	464.2539	48.3943	0.0079
0.25	0.7210	3.9482	448.1047	46.8498	0.0075
0.30	0.7079	3.9365	406.3292	42.4145	0.0070
0.35	0.7288	3.9499	390.3753	40.6508	0.0068
0.40	0.7130	4.0240	374.6174	39.1624	0.0065
0.45	0.7480	4.0258	366.6565	38.1725	0.0063
0.50	0.8728	3.8748	359.7153	36.7183	0.0068
0.55	0.7069	4.2559	353.4290	37.2933	0.0060
0.60	0.7382	4.2555	340.4038	35.7031	0.0060
0.65	0.7149	4.3387	322.6762	33.9862	0.0058
0.70	0.9057	4.0249	299.0288	30.0794	0.0063
0.75	0.7423	4.4351	303.5430	31.8139	0.0059
0.80	0.8148	4.3793	295.1566	30.4118	0.0061
0.85	0.8072	4.5002	297.2402	30.7907	0.0064
0.90	1.0137	4.2052	294.1300	29.1800	0.0073

$$\begin{aligned} K_{ij}(\dot{\varepsilon}, T) = {} & F_0 + F_1\dot{\varepsilon} + F_2T + F_3\dot{\varepsilon}T + F_4\dot{\varepsilon}^2 \\ & + F_5T^2 + F_6\dot{\varepsilon}^2T + F_7\dot{\varepsilon}T^2 + F_8T^3 \end{aligned} \tag{10}$$

where F_0, F_1, F_2, F_3, F_4, F_5, F_6, F_7, and F_8 are the fitting coefficients of the RS, and the results are listed in Table 6. Combined with the previously developed GA-SCA model, the RS-SCA model with double-coupling modification can be expressed as Eq.(11).

Table 5 K values under different thermodynamic parameters

Temperature /°C	Strain rate/s^{-1}			
	0.001	0.01	0.1	1
720	0.9855	0.9598	1.1351	1.0107
760	0.8351	1.0116	1.0271	0.9769
800	1.0835	0.9572	0.9173	0.9497
840	1.1083	1.0759	1.1223	0.9393

$$\sigma = \frac{K(\dot{\varepsilon}, T)}{\alpha(\varepsilon)}\ln\left[\left\{\frac{\dot{\varepsilon}\exp\left[Q(\varepsilon)/RT\right]}{A(\varepsilon)}\right\}^{1/n(\varepsilon)} + \left(\left\{\frac{\dot{\varepsilon}\exp\left[Q(\varepsilon)/RT\right]}{A(\varepsilon)}\right\}^{2/n(\varepsilon)} + 1\right)^{1/2}\right] \tag{11}$$

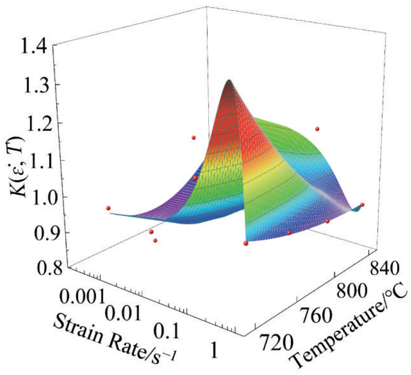

Fig.8 Nonlinear RS fitting of K-value

4 Discussion

4.1 Comparisons of established Arrhenius models

The predicted stresses corresponding to the strain range of 0.05 – 0.9 (with interval of 0.05) were calculated by the developed LR-SCA, GA-SCA, and RS-SCA models. The predicted stresses from the three Arrhenius models, under different thermodynamic parameters, are compared in detail with the experimental stresses, as shown in Fig. 9. The black solid lines represent the experimental results for hot compression under various thermodynamic parameters. The red dots, yellow square dots, and purple hexagonal dots are the results calculated by the LR-SCA, GA-SCA, and RS-SCA models, respectively. The predicted results from the three models are in good agreement with the experimental results. Meanwhile, the well-modified RS-SCA model has the highest accuracy among the LR-SCA and GA-SCA models for fitting flow stresses, especially at low deformation temperatures such as 720 and 760 °C . This demonstrates that the model's predictive accuracy for both curve profiles and derived values improves significantly after identifying optimal parameters via GA, which accounts for temperature and strain rate effects.

To more intuitively and accurately assess the prediction effect and applicability of the three Arrhenius models, five statistical indicators, namely, correlation coefficient (R), AARE, logarithm of mean squared error (ln(MSE)), relative error (δ), and standard deviation (SD), are introduced to quantitatively evaluate the prediction accuracy of the models[12,49]:

$$R = \sum_{i=1}^{n}(\sigma_{ei}-\bar{\sigma}_{e})(\sigma_{pi}-\bar{\sigma}_{p}) / \sqrt{\sum_{i=1}^{n}\left(\sigma_{ei}-\bar{\sigma}_{e}\right)^2\left(\sigma_{pi}-\bar{\sigma}_{p}\right)^2} \tag{12}$$

$$\mathrm{AARE} = \frac{1}{n}\sum_{i=1}^{n}\left|(\sigma_{pi}-\sigma_{ei})/\sigma_{ei}\right| \times 100\% \tag{13}$$

$$\ln(\mathrm{MSE}) = \ln\left[\frac{1}{n}\sum_{i=1}^{n}\left(\sigma_{pi}-\sigma_{ei}\right)^2\right] \tag{14}$$

$$\delta_i = [(\sigma_{pi}-\sigma_{ei})/\sigma_{ei}] \times 100\% \tag{15}$$

$$\mathrm{SD} = \sqrt{\frac{1}{n-1}\sum_{i=1}^{n}(\delta_i - \bar{\delta})^2} \tag{16}$$

where σ_{ei} and σ_{pi} are experimental and predicted stresses, respectively; $\bar{\sigma}_e$ and $\bar{\sigma}_p$ are the mean values of σ_{ei} and σ_{pi}, respectively; n is the total number of samples.

Table 7 summarizes the aforementioned statistical indicators for the three models. The R, AARE, and ln(MSE) values of the LR-SCA model are 0.9902, 7.0074%, and 4.9318, respectively. The R, AARE, and ln(MSE) values of the GA-SCA model are 0.9893, 6.3048%, and 5.0975, respectively. The R, AARE, and ln(MSE) values of the RS-SCA model are 0.9980, 2.1560%, and 3.3343, respectively. Comparing the results of the above indicators, the RS-SCA model's R value is the highest, and its AARE and ln(MSE) values are the smallest. Generally, higher R values (close to 1) and lower AARE and ln(MSE) values (close to 0) indicate higher predictive accuracy and better model fit. Fig. 10 shows another comparison between the experimental and predicted results. For the three models, most data points cluster around the best-fit line and within the ±10% deviation region (purple). Among the three models, the RS-SCA model's data points are more densely clustered around the best-fit line. Therefore, the RS-SCA model provides the best correlation and accuracy in predicted results compared to other models.

In addition, the accuracy of the developed three SCA models was further evaluated by statistically analyzing δ and SD between the experimental and predicted stresses. The results are presented as frequency histograms, as shown in Fig. 11. The statistical analysis shows that the δ values of the three models follow a typical normal distribution. LR-SCA model shows the maximum error dispersion (−14.84%–22.42%), while the error ranges of the GA-SCA (−15.14%–21.97%) and RS-SCA (−12.86%–19.21%) models gradually converge after parameter optimization and RS correction. The LR-SCA model achieves 86.8% of predictions with ±10% error. The GA-SCA model improves this indicator to 88.9%, and the RS-SCA model improves it to 97.9%. Furthermore, compared with the LR-SCA and GA-SCA models, the RS-SCA model shows a significant reduction in both the AARE and the SD. This further validates the superior predictive performance of the RS-SCA model for TC18 alloy flow stress, demonstrating higher accuracy than the LR-SCA and GA-SCA models, consistent with prior conclusions.

Compared with the LR-SCA and GA-SCA models, the core advantage of the RS-SCA model lies in the RS correction term $K_{ij}(\varepsilon, T)$, which effectively addresses the inherent limitations of the other two models. The LR-SCA model, based on LR, can only describe simple linear relationships between flow stress and variables such as temperature, and fails to accurately capture the complex nonlinear hot deformation behavior of TC18 alloy. Although the GA-SCA model

Table 6 Fitting coefficients for RS

F_0	F_1	F_2	F_3	F_4	F_5	F_6	F_7	F_8
22.7390	0.5810	−0.0637	0.0183	−13.3620	5.4240×10^{-5}	0.0164	-2.3420×10^{-5}	-1.0740×10^{-8}

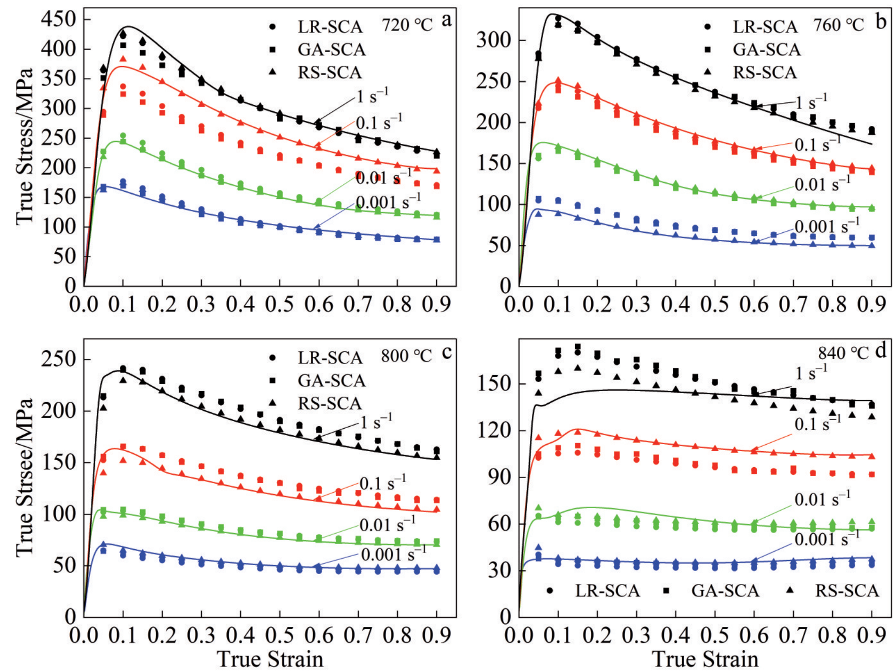

Fig.9 Comparison of experimental values and predicted values of three models at different thermodynamic parameters: (a) 720 °C; (b) 760 °C; (c) 800 °C; (d) 840 °C

Table 7 Values of evaluation indicators of three models

Model	R	AARE/%	ln(MSE)
LR-SCA	0.9902	7.0074	4.9318
GA-SCA	0.9893	6.3048	5.0975
RS-SCA	0.9980	2.1560	3.3343

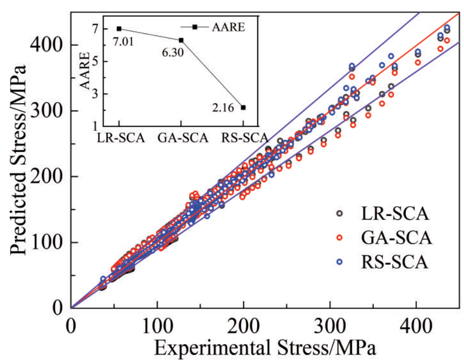

Fig.10 Correlation analysis of LR-SCA, GA-SCA, and RS-SCA models

optimizes the Arrhenius parameters, it still treats temperature, and strain rate as independent variables, neglecting their synergistic influence during deformation. In contrast, the $K_{ij}(\varepsilon, T)$ term in the RS-SCA model is constructed by fitting the deviations between GA-SCA model predictions and experimental data, thereby enabling it to accurately capture the interaction between temperature and strain rate. For instance, temperature has a greater effect on flow stress at low strain rates, whereas its influence is weaker at high strain rates. This precise characterization of the coupling effect significantly reduces prediction errors, resulting in a narrower error distribution and higher prediction accuracy for the RS-SCA model compared to the other two models.

4.2 FE verification

After incorporating GA-optimized parameters and temperature-strain-rate coupling compensation mechanisms, the RS-SCA model demonstrates significantly improved accuracy in characterizing the hot deformation behavior of the TC18 alloy. However, to validate its reliability in industrial applications, the model still requires secondary development within FE software to simulate TMP processes.

The geometrical models of a workpiece (Φ10 mm×15 mm) and two anvils (Φ20 mm×5 mm) were created in UG 12.0 and imported into DEFORM-3D in STL format. A nonlinear thermomechanically coupled FE model for the hot compression test was established, in which the cylindrical workpiece and anvils were defined as plastic and rigid bodies, respectively. The shear friction coefficient between the anvil and the workpiece was set to 0.3, and the workpiece was divided into 100 000 tetrahedral mesh elements. Heat radiation and heat conduction between objects were considered to simulate real experimental conditions. The initial temperature is consistent with the experimental settings. In the motion setup module, the bottom anvil is fixed, and the movement velocity of the top anvil is set by the time-control mode. The relationship between the velocity and the strain rate can be simplified as Eq.(17)[12]:

$$v = H_0 \dot{\varepsilon} \exp\left(-\dot{\varepsilon} t\right) \tag{17}$$

where v is the movement velocity of the top anvil, H_0 is the initial height of the specimen, and t is the movement time of the top anvil. Hot compression tests were simulated in

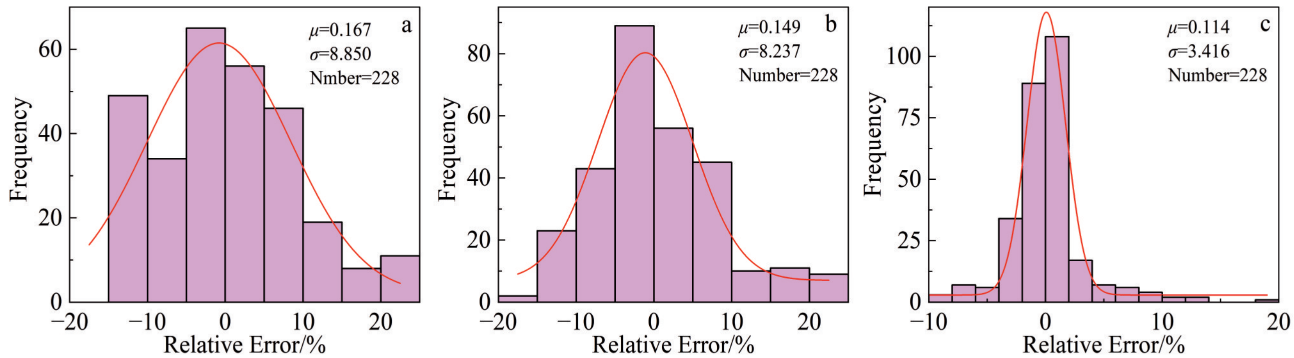

Fig.11 Relative error distribution of the three models: (a) LR-SCA; (b) GA-SCA; (c) RS-SCA

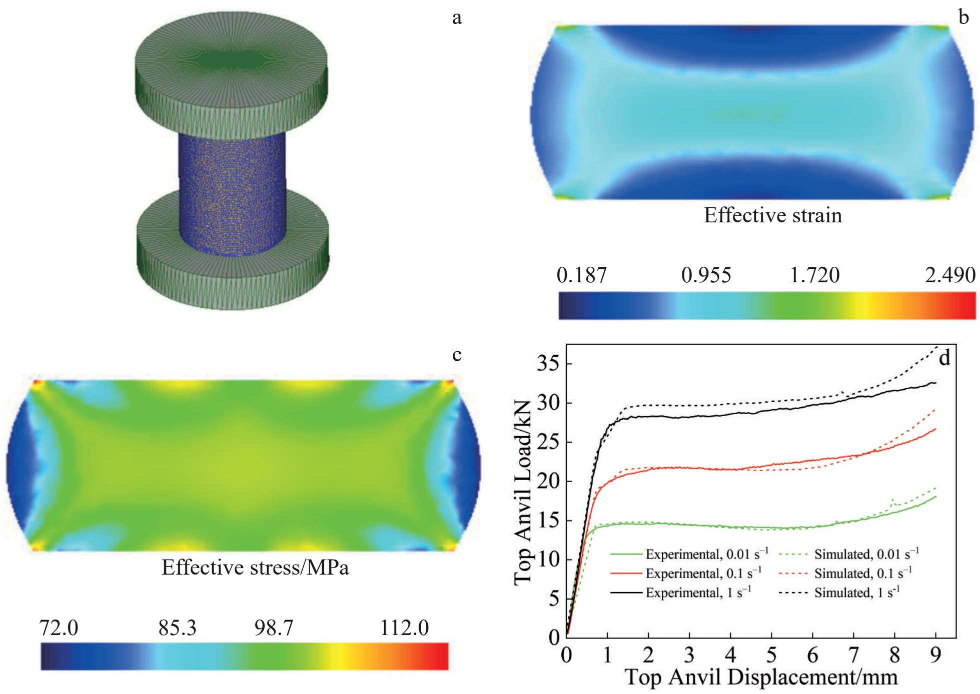

Fig.12 FE simulation model and simulation results of TC18 alloy hot compression using DEFORM-3D: (a) 3D FE model, (b) effective strain distribution, (c) effective stress distribution at 760 °C/0.01 s^{-1}/60%, and (d) comparison between simulated and experimental top anvil load-displacement curves

DEFORM-3D at a deformation temperature of 760 °C and strain rates of 0.01, 0.1, and 1 s^{-1}, with a 60% height reduction. Their equivalent stress distribution and force-load curves were investigated for the four forming conditions.

Fig. 12 presents the FE model generated by the developed RS-SCA model and the corresponding simulation results. A clear axisymmetric pattern is observed in both effective strain and effective stress distributions across the diameter surface of the specimen. Quantitative analysis reveals significant regional variations in strain, with an average value of 0.899, as shown in Fig.12b. The strain field shows three deformation zones: large deformation, small deformation, and difficult deformation, which directly correlate with the observed stress inhomogeneity (Fig. 12c). This heterogeneous deformation behavior manifests as a characteristic bulging morphology in the compressed specimen. Therefore, the simulated physical quantities agree well with the experimental results.

In addition, the close correspondence between simulated and experimental mechanical responses throughout the thermal compression process is particularly noteworthy. At the specified processing temperature of 760 °C, simulations yield load-displacement curves that are remarkably consistent with experimental measurements across various strain rates, with maximum load deviations of up to 5%. These comparative results comprehensively validate the reliability and practical applicability of the RS-SCA model in TMP simulations of TC18 alloy. The model's enhanced predictive capability stems from its novel integration of parameter optimization with coupled multi-physics interactions, establishing a new paradigm for iterative process optimization in TMP simulations.

5 Conclusions

1) The flow stress of TC18 alloy exhibits a strong correlation with thermodynamic parameters: it decreases with increasing deformation temperature and increases with increasing strain rate.

2) The LR-SCA model is developed using LR, with strain effects incorporated through a 9th-order polynomial fit. The model parameters are further optimized using an advanced GA framework, with the search space defined by LR-SCA parameter ranges and residual errors serving as the fitness function.

3) To enhance accuracy, an RS fitting function is applied to modify the GA-SCA model quadratically, resulting in an RS-SCA model that accurately captures the hot deformation behavior of TC18 alloy. Evaluation using multiple statistical indicators (R, AARE, ln(MSE), δ, and SD) confirms that the RS-SCA model exhibits the strongest predictive capability and the smallest error, demonstrating excellent agreement with experimental data.

4) The RS-SCA model is successfully integrated into DEFORM-3D through secondary development for simulating hot compression tests. The close agreement between simulated field distributions, load-displacement curves, and experimental results verifies the model's reliability in FE numerical simulations.

References

1 Fan X G, Yang H, Gao P F *et al. Journal of Materials Processing Technology*[J], 2016, 234: 290
2 Zhao Q Y, Sun Q Y, Xin S W *et al. Materials Science and Engineering A*[J], 2022, 845: 143260
3 Dong R F, Li J S, Kou H C *et al. Journal of Materials Science & Technology*[J], 2019, 35(1): 48
4 Ge J Y, Shi S X, Zhan X D *et al. Materials Science and Engineering A*[J], 2024, 911: 146857
5 Ge J Y, Shi S X, Zhan X D *et al. Journal of Alloys and Compounds*[J], 2025, 1010: 178149
6 Li C M, Huang L, Zhao M J *et al. Journal of Alloys and Compounds*[J], 2022, 905: 164161
7 Gao P F, Zhan M, Fan X G *et al. Materials Science and Engineering A*[J], 2017, 689: 243
8 Guo J, Zhan M, Wang Y Y *et al. Journal of Alloys and Compounds*[J], 2018, 767: 34
9 Fan J K, Kou H C, Lai M J *et al. Materials & Design*[J], 2013, 49: 945
10 Shi S X, Ge J Y, Zhang X Y *et al. Journal of Materials Research and Technology*[J], 2024, 33: 8329
11 Li C M, Huang L, Zhao M J *et al. Materials Science and Engineering A*[J], 2021, 814: 141231
12 Shi S X, Liu X S, Zhang X Y *et al. Transactions of Nonferrous Metals Society of China*[J], 2021, 31(6): 1665
13 Ding S L, Gao S, Jiang X *et al. Materials Today Communications*[J], 2025, 42: 111230
14 Li C M, Huang L, Li C L *et al. Rare Metals*[J], 2022, 41(5): 1434
15 Liu R E, Wang B Y, Hu S S *et al. Journal of Materials Research and Technology*[J], 2023, 24: 4904
16 Xia Y X, Shu X D, Zhang Q D *et al. Journal of Materials Research and Technology*[J], 2023, 26: 1325
17 Man Y Y, Zhang H Y, Cheng J *et al. JOM*[J], 2024, 77: 774
18 Wu Y, Wang D J, Liu Z Q *et al. International Journal of Mechanical Sciences*[J], 2019, 164: 105126
19 Bobbili R, Ramudu B V, Madhu V. *Journal of Alloys and Compounds*[J], 2017, 696: 295
20 Sellars C M, McTegart W J. *Acta Materialia*[J], 1966, 14(9): 1136
21 Johnson G R, Cook W H. *Engineering Fracture Mechanics*[J], 1983, 21: 541
22 He Z B, Wang Z B, Lin Y L *et al. Metals*[J], 2019, 9(2): 243
23 Zerilli F J, Armstrong R W. *Journal of Applied Physics*[J], 1987, 61(5): 1816
24 Zhang J Q, Di H S. *Materials Science and Engineering A*[J], 2016, 676: 506
25 Liu X J, Zhang H Y, Zhang S *et al. Journal of Alloys and Compounds*[J], 2023, 968: 172052
26 Kumar S, Pradhan H, Shah N *et al. Scripta Materialia*[J], 2023, 234: 115543
27 Qi C, Niu Y Z, Chen X L *et al. Rare Metal Materials and Engineering*[J], 2026, 55(4): 941
28 Deng C Y, Dong S J, Tan W *et al. Materials Research Express*[J], 2019, 6(2): 029544
29 Shi S X, Ge J Y, Zhang X Y *et al. Journal of Materials Research and Technology*[J], 2024, 28: 3722
30 Jiang F, Fei L Y, Jiang H *et al. Journal of Materials Research and Technology*[J], 2023, 23: 1062
31 Chai Z, Wang W Y, Ren Y *et al. Materials Science and Engineering A*[J], 2024, 898: 146331
32 Wang L, Li W, Jin P P *et al. Journal of Materials Research and Technology*[J], 2023, 23: 3602
33 Xia Y F, Jiang W, Cheng Q *et al. Transactions of Nonferrous Metals Society of China*[J], 2020, 30(1): 134
34 Long S, Xia Y F, Wang P *et al. Journal of Alloys and Compounds*[J], 2019, 796: 65
35 Robson J D, Armstrong D, Cordell J *et al. Mechanics of Materials*[J], 2024, 189: 104881
36 Li J L, Wang B Y, Huang H *et al. Journal of Alloys and Compounds*[J], 2018, 748: 1031
37 Shi S X, Ge J Y, Lin Y C *et al. Materials Science and Engineering A*[J], 2022, 847: 143335
38 Jiang Y Q, Lin Y C, Jiang X Y *et al. Materials Characterization*[J], 2020, 163: 110272
39 Gao P F, Fu M W, Zhan M *et al. Journal of Materials Science & Technology*[J], 2020, 39: 56
40 Shi Z Y, Quan G Z, Chao A N *et al. Transactions of Nonferrous*

Metals Society of China[J], 2019, 29(10): 2090

41 Wu Y, Kou H C, Tang B *et al. Advanced Engineering Materials*[J], 2018, 20(2): 1700587

42 Yu S, Zhang H, Wan Z P *et al. Transactions of Nonferrous Metals Society of China*[J], 2019, 29(3): 546

43 Dong X J, Hu S S, Xu Y *et al. Transactions of Nonferrous Metals Society of China*[J], 2021, 31(4): 858

44 Li L, Li M Q, Luo J. *Materials Science and Engineering A*[J], 2015, 628: 11

45 Li L, Luo J, Yan J J *et al. Journal of Alloys and Compounds*[J], 2015, 622: 174

46 Long J C, Xia Q X, Xiao G F *et al. International Journal of Mechanical Sciences*[J], 2021, 191: 106069

47 Huang C Q, Jia X D, Zhang Z W. *Materials*[J], 2018, 11(5): 855

48 Halder C, Sitko M, Madej L *et al. Materials Science and Technology*[J], 2016, 32(4): 366

49 Niu L Q, Cao M, Liang Z L *et al. Materials Science and Engineering A*[J], 2020, 789: 139612

采用遗传算法与响应面法改进的TC18合金应变补偿Arrhenius模型

丁少玲[1]，吴　茗[1]，史双喜[2,3]，安　惠[1]，张　勇[2,3]

（1. 桂林理工大学 数学与统计学院，广西 桂林 541006）

（2. 桂林航天工业学院 广西特种工程装备与控制重点实验室，广西 桂林 541004）

（3. 桂林航天工业学院 广西贵金属新材料先进流程制造工程研究中心，广西 桂林 541004）

摘　要：热变形行为的准确预测对钛合金锻件的数值模拟与智能制造至关重要。通过Gleeble-3800热模拟试验机，在720~840 ℃温度范围和0.001~1 s^{-1}应变速率下对TC18合金进行等温压缩试验，研究了其高温变形特性。为精确描述流变行为，逐步构建并对比评估了3种应变补偿Arrhenius本构模型（SCA）：基于线性回归拟合的传统模型（LR-SCA）、遗传算法优化模型（GA-SCA）以及响应面修正模型（RS-SCA）。结果表明，遗传算法优化能有效识别全局最优参数，而响应面修正成功考虑了温度与应变速率的耦合效应。统计评估显示，RS-SCA模型具有最优的预测能力，其相关系数（R）达0.9980，平均绝对相对误差仅为2.16%，相较于LR-SCA模型的7.01%显著降低。通过在DEFORM-3D软件中对所建立的RS-SCA模型进行二次开发，进一步验证了其可靠性——在稳定工艺条件下的有限元模拟结果与实验载荷-位移曲线高度吻合。该稳健的本构模型为TC18合金构件在热机械加工应用中的有限元模拟与工艺优化奠定了坚实的基础。

关键词：TC18合金；流变应力；热变形行为；Arrhenius本构模型；有限元模拟

作者简介：丁少玲，女，1983年生，博士，副教授，桂林理工大学数学与统计学院，广西　桂林　541006，E-mail：dingshl@glut.edu.cn